https://doi.org/10.5194/egusphere-2026-4436
Preprint. Discussion started: 23 September 2026

Morphologically complex ice crystal plate structures in mid-latitude cirrus: combining space-borne lidar, in-situ scattering, and physical optics simulation

Harry Ballington[1], Martin Schnaiter[1], and Emma Järvinen[1]

[1]Institute for Atmospheric and Environmental Research, University of Wuppertal, Germany

Correspondence: Harry Ballington (ballington@uni-wuppertal.de)

Abstract. The scattering properties of ice crystals in cirrus clouds are critical for interpreting lidar observations, yet practical retrievals focus on idealised habits representing fewer than 10 % of natural cirrus, leaving the irregular and aggregated geometries that dominate real clouds poorly constrained. This study combines three independent lines of evidence to identify which habits are most consistent with mid-latitude cirrus observations: lidar and depolarisation ratios from the EarthCARE ATLID high-spectral-resolution lidar, in-situ angular scattering and stereographic imaging from the PHIPS probe during CIRRUS-HL, and physical geometric optics simulations of hexagonal plates, intersecting plate aggregates, and touching plate aggregates with surface roughness. Both datasets cover the same mid-latitude region and the in-situ data provides about 12,000 manually classified plate, side-plane, and aggregate particles across 22 flights. For each habit and roughness level, orientation- and ensemble-averaged scattering properties are simulated for 1000-particle ensembles with sizes drawn from the measured distribution. All three pristine habits produce lidar and depolarisation ratios within the observed range, but any roughening of the single plate habit drives the lidar ratio away from most observations, attributed to loss of retroreflective backscattering. Touching plate aggregates remain consistent across all roughness levels, owing to diffuse scattering from their open structures. The angular scattering function alone does not distinguish habits, but combined with the lidar constraints it identifies smooth intersecting aggregates and roughened touching aggregates as the most plausible dominant backscatterers. The extent to which these ratios can discriminate habit composition is discussed.

1 Introduction

Cirrus clouds cover on average 30 % of the Earth's surface, up to 70 % in the tropics, and have a large impact on climate evolution and radiation balance in the atmosphere (Li and Groß, 2022). The properties of the ice crystals within them are among the largest sources of uncertainty in radiative equilibrium climate sensitivity, the likely range of which has barely narrowed in over four decades of research (Charney et al., 1979; IPCC, 2021). Where that sensitivity falls carries direct consequences for the rate of sea level rise, the frequency of extreme weather, and the viability of international climate targets.

It is known that both the sign and strength of the radiative forcing and feedback due to cirrus are sensitive to several parameters, including geography, season, time of day, and dynamical setting. Collectively, these factors influence the concentrations, shapes, sizes, and surface textures of the ice particles in the cloud (Burkhardt and Kärcher, 2011; Harrington et al., 2009; Järvi-

https://doi.org/10.5194/egusphere-2026-4436
Preprint. Discussion started: 23 September 2026

nen et al., 2018a; Yi et al., 2016; Magee et al., 2021). Recently, attention has been directed towards evaluating the fundamental uncertainties associated with cirrus microphysical compositions and their life-cycle evolution within the cloud, something that can be obscured by the complexity of modern satellite retrieval schemes (Hioki et al., 2016; Saito et al., 2017; Magee et al., 2021). The ice habit and degree of surface roughness are thought to have a non-negligible effect on the radiative properties of cirrus (Baran, 2009; Cole et al., 2014; Järvinen et al., 2023), and it is often cited that surface roughness can lead to a doubling in reflected solar energy from cirrus (Baran, 2012). However, this statement rests on laboratory derived asymmetry parameter measurements in which the uncertainty was not quantified (Ulanowski et al., 2006).

1.1 Physical optics and coherent backscattering

Using numerically exact light-scattering methods to compute accurate optical properties of realistic ice crystals incurs large and sometimes infeasible computational costs, particularly in the shortwave spectral regime. Classical geometric optics (GO) has been widely used in the literature for over 25 years (Hess and Wiegner, 1994; Yang and Liou, 1996; Macke et al., 1996), but lacks the accuracy for computing ice crystal backscattering properties due to inherent limitations. These include a lack of consideration of coherent backscattering enhancement (CBE), as well as singularities associated with collimated rays emerging from parallel-facet retroreflections (Saito and Yang, 2023; Zhou and Yang, 2015). To resolve these limitations, Physical Optics (PO) methods have been developed, which utilise some form of the electromagnetic equivalence theorem (Bi et al., 2011; Saito and Yang, 2023; Konoshonkin et al., 2015). PO methods also account for the size-dependent nature of the particle scattering problem by using a numerically accurate surface or volume integral equation.

The behaviour of the coherent backscattering peak in small particles has been studied for some time (Muinonen et al., 1989). More recently, Zhou and Yang (2015) used rigorous numerical simulations to predict the presence of a coherent backscattering peak for smooth regular, smooth irregular, and roughened hexagonal ice crystals. The width of the peak was found to be governed by Fraunhofer diffraction of the backscattered plane-parallel beams and is proportional to λ/L, where L is a characteristic minimum dimension such as the plate thickness or column cross-section diameter (Borovoi and Grishin, 2003; Zhou and Yang, 2015). They confirmed that GO fails to produce the expected backscattering phase function behaviour for roughened ice crystals as derived from CALIOP observations (Baum et al., 2011). They attributed this to surface roughness, which suppresses the corner-reflection effect, leaving GO methods with no mechanism to generate the observed backscattering peak. Zhou (2018) then devised a theoretical treatment of the coherent backscattering peak using a recursive relations solution of Maxwell's equations. By comparing reverse terms in the summation, the origin of the coherent backscattering enhancement was studied, which manifests when the particle exceeds a certain size, with the enhancement factor varying between 1 and 2. Capturing this effect in a model requires careful treatment of phase in the outgoing and internal waves. Examples of physical optics methods that can achieve this include those by Borovoi and Grishin (2003), Borovoi et al. (2014), Bi et al. (2011), and Hesse et al. (2018). The effects of coherent backscattering in radiative transfer applications have also been simulated using the RT-CB code (Muinonen, 2004; Markkanen and Penttilä, 2023), in which a combination of ladder and cyclical diagrams represent the standard vector radiative transfer equation and the constructive interference at backscattering due to conjugate scattering paths, respectively (Muinonen et al., 2012). By analogy, Borovoi et al. (2019) showed that the backscattered light

https://doi.org/10.5194/egusphere-2026-4436
Preprint. Discussion started: 23 September 2026

from a single large irregular particle can be separated into coherent and incoherent components. When the particle shape contains dihedral angles of 90°, as in pristine hexagonal crystals, an additional incoherent backscattering peak arises from the corner-reflection effect, with a width proportional to λ divided by the transverse size of the backscattered beams. A simplified CBE correction was introduced by Saito and Yang (2023) into the Improved Geometric Optics Method (IGOM)+CBE. The correction accounts for coherent backscattering enhancement at 180°, but introduces a discontinuity in the phase matrix at the backscattering direction (Zhou et al., 2025). The (IGOM)+CBE results agree with numerically exact methods at a single moderate roughness level, but show more disagreement for smooth and severely roughened columns.

1.2 Surface roughness and depolarisation

It has been shown by both simulation (Saito and Yang, 2023) and theoretical calculations (Mishchenko and Sassen, 1998) that for larger size parameters, surface roughness leads to an increase in the depolarisation ratio. The values range from around 0.2 for smooth particles to values approaching 0.6 for severely roughened particles. This knowledge explains, to some degree, the wide range of depolarisation ratios measured in cirrus clouds. Saito and Yang (2023) noted that their quantitative interpretation of the effects of surface roughness on backscattering properties was limited to compact hexagonal column ice crystals with unity aspect ratio, and that further studies with various macroscopic shapes was necessary. The present study extends this research to hexagonal plates and aggregates of plates, taking the next step towards improving polarimetric lidar observation characterisation of ice cloud morphological and microphysical properties.

1.3 Lidar-based habit discrimination

An attractive reason for a comprehensive understanding of how particle shape and surface texture affect scattering is for the interpretation and retrieval of cloud properties from experimental data. In an ideal scenario, the full scattering properties of an ice cloud would be directly measurable (either in-situ or by ground or airborne remote sensing), providing the input needed for downstream radiative transfer calculations. In practice, only a subset of the scattering information is directly accessible from any single measurement, and the remaining properties must be inferred through simulation. Measurement and simulation are therefore symbiotic in determining the optical properties of ice clouds. Habit classification has historically served as a practical simplification, reducing the problem to a discrete set of representative particle types for which scattering properties can be precomputed. With the increasing availability of computational resources, the need for such simplification is diminishing, but the framework remains embedded in current retrieval algorithms and operational products.

As an example of the use of ice crystal habits in recent literature, Okamoto et al. (2019) used PO modelling to estimate the backscattering coefficient β, lidar ratio S, and depolarisation ratio δ of five randomly oriented three-dimensional ice particle shapes and two quasi-horizontally oriented particle types at 355 nm. They found that β can vary by more than an order of magnitude among particle types with the same effective radius, and by two orders of magnitude at large sizes ($r_{\text{eff}} = 1000\,\mu\text{m}$). They concluded that both S and δ are needed for distinguishing among particle habits and orientations. However, the S–δ diagram has limitations when applied to mixed-habit clouds, because the bulk lidar signal is dominated by particles with the largest backscattering cross section, which restricts the ability to discriminate the full range of habits present. The S–δ frame-

https://doi.org/10.5194/egusphere-2026-4436
Preprint. Discussion started: 23 September 2026

work has since been adopted operationally in the JAXA Level 2 cloud products for the EarthCARE (Earth Clouds, Aerosols and Radiation Explorer) mission, where retrieved lidar ratio and depolarisation ratio are used to classify ice particles into habit categories including plates, columns, bullet rosettes, droxtals, and irregular or roughened types (Sato et al., 2025; Okamoto et al., 2019). This approach is discussed further in Sect. 4.4. Another application is the scattering database of Yang et al. (2013), which spans 11 ice crystal habits, a wavelength range from 0.2–100 μm, 189 particle sizes, and a limited set of degrees of surface roughness (smooth, moderate, and severe). The scattering is computed using a combination of the discrete dipole approximation (ADDA) (Yurkin and Hoekstra, 2011), T-matrix, and IGOM. Comparison with satellite polarimetric observations showed that the severely roughened ice crystal models significantly outperform their smooth counterparts (Yang et al., 2013). Despite this, the habit classification within the EarthCARE Level 2 products is based on scattering computations for pristine, smooth particle surfaces (Okamoto et al., 2019). As noted by Saito and Yang (2023), Ballington and Hesse (2024a), and others, backscattering properties are highly sensitive to the presence of surface roughness. While integrated scattering properties over the full angular range are also affected, the changes are modest in comparison to the effect at individual scattering angles, where even small amounts of surface roughness relative to an idealised pristine shape can alter the scattering by an order of magnitude or more. The choice of computational method alone can vary the backscattering by at least 50 %. Greater emphasis is therefore required in future literature on providing uncertainty estimates for values derived from approximate methods such as the various implementations of physical optics and geometric optics integral equation methods.

1.4 Observational evidence for irregular ice

There is growing evidence, most of it indirect or from remote sensing, that atmospheric ice crystals tend to have shapes departing from idealised geometries based on perfect hexagonal prisms (Ulanowski et al., 2014; Schnaiter et al., 2016; Järvinen et al., 2018a, b). Using in-situ two-dimensional scattering pattern measurements from the Small Ice Detector 3 (SID-3) probe, which covers scattering angles from 6–25°, Ulanowski et al. (2014) found that the patterns obtained in cirrus and mixed-phase clouds were typically characterised by pronounced speckle, consistent with ice particles having highly irregular or rough surfaces. They also reported that the transition from smooth to roughened ice analogue crystals, measured using a levitation technique, lowered the asymmetry parameter from 0.81 to approximately 0.63 (Ulanowski et al., 2006), corresponding to almost a doubling of the reflectivity of a cloud composed entirely of such particles; a similar lowering was found for mineral dust grains (McCall, 2011). However, these measurements did not cover the full phase function, and the associated uncertainty was not quantified. A small deviation from an idealised pristine hexagonal shape, even a perturbation with amplitude small compared to the wavelength, can have substantial implications for the shape of the phase function while the asymmetry parameter remains largely unchanged.

The PHIPS (Particle Habit Imaging and Polar Scattering) instrument for the HALO research aircraft was designed for simultaneous stereographic imaging of single ice crystal microphysics and measurement of the angular scattering function (Schnaiter et al., 2018). The capability to characterise particles from in-situ measurement presents the opportunity for constraining the radiative properties across ice crystal habits. For instance, Schnaiter and Järvinen (2026) found that the scattering properties of visually pristine particles can only be reproduced by models when a finite degree of surface roughness is included. The

https://doi.org/10.5194/egusphere-2026-4436
Preprint. Discussion started: 23 September 2026

findings reinforce the idea that idealised, optically smooth surfaces are rarely found in atmospheric conditions. Analysis of SID-3 two-dimensional scattering patterns by Järvinen et al. (2018a), using speckle texture analysis to quantify ice crystal complexity, found that between 61 % and 81 % of atmospheric ice crystals sampled across several campaigns are complex in shape, with relatively flat, featureless angular scattering patterns characteristic of geometries with roughened surfaces. It is frequent in observations to find an absence of the 22° and 46° halo angles in ice crystal scattering functions (C. Labonnote et al., 2000; Auriol et al., 2001; Jourdan et al., 2003), reinforcing the idea that idealised hexagonal prism geometries are rarely found in nature.

1.5 Outline

The preceding subsections establish that (i) physical optics methods are preferable over classical geometric optics calculations, since they can account for the coherent backscattering peak and the size-dependent nature of scattering; (ii) while the sensitivity of backscattering to surface roughness has been quantified for hexagonal columns, the influence on other ice crystal habits is largely uninvestigated; and (iii) observational evidence indicates that the majority of atmospheric ice crystals are irregular or roughened.

This study addresses these gaps by combining three independent lines of evidence. In Sect. 2, two observational datasets are described: (1) EarthCARE ATLID high-spectral-resolution lidar retrievals of lidar ratio and depolarisation ratio at 355 nm, and (2) in-situ angular scattering and stereographic imaging from the PHIPS probe during the CIRRUS-HL campaign. Sect. 3 details physical geometric optics simulations of hexagonal plates, intersecting plate aggregates, and touching plate aggregates with varying amounts of surface roughness, computed for 1000-particle ensembles with sizes drawn from the measured distribution. In Sect. 4, simulated lidar ratio and depolarisation ratio trajectories are compared against ATLID retrievals, and the angular scattering profiles are compared against the PHIPS measurement. Sect. 5 summarises the findings and identifies which ice crystal habits are most consistent with the observed mid-latitude cirrus, towards improved representation of ice cloud radiative properties in future retrieval and climate modelling frameworks.

2 Observational data

This study combines in-situ PHIPS measurements from the 2021 CIRRUS-HL campaign with 2025 data from the EarthCARE (Earth Clouds, Aerosols and Radiation Explorer) mission. The in-situ measurements provide direct particle-level observations of ice crystal habit, size, and angular scattering, while the satellite data provides bulk backscatter-weighted lidar ratio and depolarisation ratio retrievals. The geographic coverage of both datasets is shown in Fig. 1, spanning a mid-latitude region over the Arctic, North Atlantic, Central Europe, Scandinavia, and Iceland.

2.1 CIRRUS-HL and PHIPS

The CIRRUS-HL (Cirrus in High Latitudes) campaign targeted cirrus clouds over the Arctic, North Atlantic, Central Europe, Scandinavia, and Iceland, with a total cloud sampling time of approximately 34 h across 22 flights from 24 June to 29 July

https://doi.org/10.5194/egusphere-2026-4436
Preprint. Discussion started: 23 September 2026

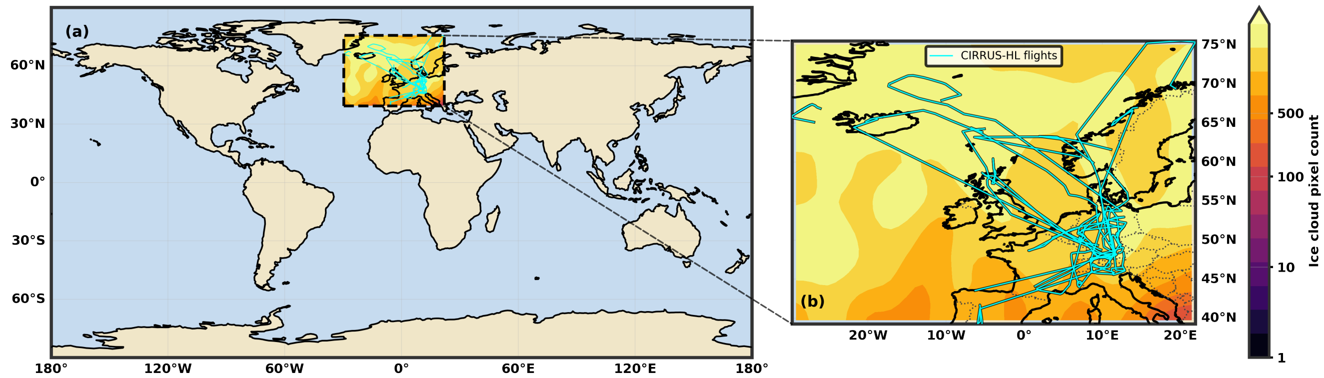

Figure 1. Geographic coverage of ATLID ice cloud observations and CIRRUS-HL flight tracks. (a) Global view showing ATLID observation density (filled contours) within the CIRRUS-HL longitude and latitude range (dashed box), with flight tracks overlaid in cyan. (b) Zoomed view of the CIRRUS-HL campaign region with coastlines, national borders, and individual flight tracks. The colour scale indicates the smoothed ice cloud pixel count per spatial bin.

2021. The HALO (High Altitude and Long Range) research aircraft, a modified Gulfstream G550 operated by the Deutsches Zentrum für Luft- und Raumfahrt (DLR, German Aerospace Center) based at Oberpfaffenhofen, Germany, carried in-situ cloud instrumentation including the PHIPS probe (Schnaiter et al., 2018). The PHIPS probe measures scattered light at 532 nm across an angular range of 18–170° and provides 5 µm resolution stereographic imaging of individual ice particles. The imaging setup enables classification of ice particle habit, while the measured scattering provides opportunity for validation against theoretical light scattering models. The instrument's detectable size range is approximately 20–800 µm. The range of in-situ measurements cover a mid-latitude/polar latitudinal range of 39.3–75.5° N.

2.1.1 Habit classification and height dependence

The height-resolved in-situ observations are shown in Fig. 2a–d, clipped to the 1st and 99th percentile altitude range of the classified CIRRUS-HL particles. The dataset comprises over 63 000 images manually classified into habit categories; panels (a)–(d) represent the classified particle fraction. Ambient temperature shows a fairly linear increase with decreasing altitude. The habit categories shown in panel (c) are grouped as follows: "Plate-like" includes plates, side-planes, sectored plates, skeleton plates, and polycrystalline plate variants; "Column-like" includes columns, capped columns, and polycrystalline column variants; "Bullet Ros." includes bullet rosettes and mixed rosettes; "Frozen Drop." includes single frozen droplets and their chain and aggregate structures; "Other" includes classified habits such as dendrites, needles, graupel, as well as particles that were examined but did not fall under the other habits. In general, each habit contains single-crystal and poly-crystal particles. Excluding the "Other" category, plate-like structures constitute the largest habit fraction across the sampled altitude range. The particle size distribution in panel (d) is row-normalised and smoothed with a Gaussian filter ($\sigma = 2$ bins) to better show the qualitative distribution. For additional analysis of the habit classification, the reader is referred to Järvinen and Schnaiter (2026).

https://doi.org/10.5194/egusphere-2026-4436
Preprint. Discussion started: 23 September 2026

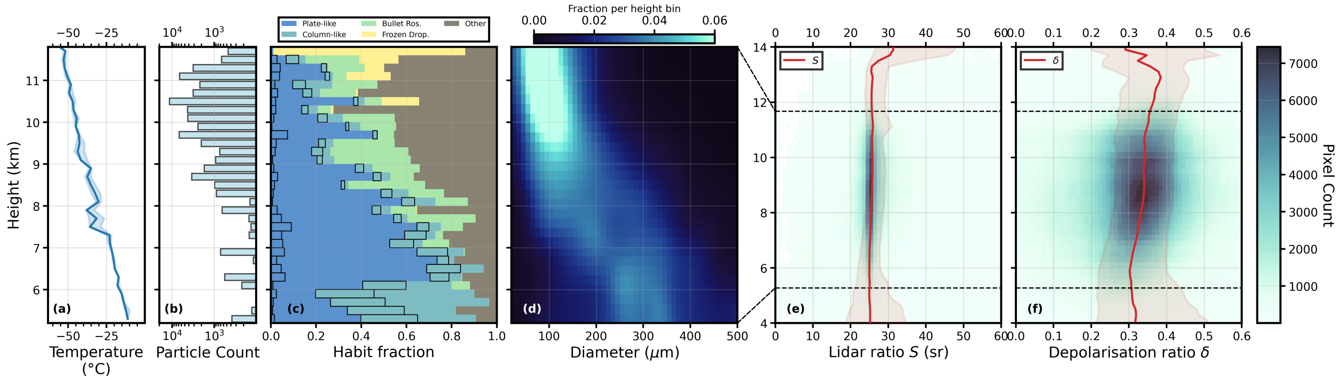

Figure 2. Observations from the two campaigns as a function of height. (a) Ambient temperature. (b) Classified particle count. (c) Fractional habit composition. Rectangular outline indicates the fraction of single particles in the plate and column-like habits. (d) Row-normalised particle size distribution. (e) Median retrieved lidar ratio S. (f) Median retrieved depolarisation ratio δ. Dashed lines in panels (e) and (f) indicate the 1st and 99th percentile range of the CIRRUS-HL observations.

For this work, approximately 12 000 plate-like particles are selected for further analysis, comprising three categories: 1706 single plates with mean diameter $105 \pm 51\,\mu\mathrm{m}$, 5700 plate aggregates with mean diameter $178 \pm 84\,\mu\mathrm{m}$, and 4398 side-planes with mean diameter $169 \pm 82\,\mu\mathrm{m}$. Example stereographic images from the PHIPS camera system are shown in the top row of Fig. 3, illustrating single plate, plate aggregate, and side-plane morphologies. The justification for focusing on plate-like habits in the subsequent simulation is discussed further in Sect. 3.2.

2.2 EarthCARE and ATLID

The EarthCARE mission is a European Space Agency and Japan Aerospace Exploration Agency (JAXA) cooperation, with the goal of measuring the vertical and horizontal distribution of cloud and aerosol fields, as well as outgoing radiation, in order to evaluate their representation in weather and climate models (Wehr et al., 2023). The EarthCARE satellite launched on 28 May 2024 from Vandenberg Space Force Base, California. The satellite orbits at a mean altitude of 393 km in a sun-synchronous orbit with inclination 97.05°, orbital period 92.5 min, and a repeat cycle of 25 days. The EarthCARE payload consists of four complementary instruments: the Atmospheric Lidar (ATLID), Cloud Profiling Radar (CPR), Multi-Spectral Imager (MSI), and Broad-Band Radiometer (BBR). The ATLID instrument is the first high-spectral-resolution lidar (HSRL) to be launched into space. Compared to previous spaceborne lidar missions, the HSRL technology allows for separation of molecular and particulate backscattering, which in principle enables better constraint on retrieval compared to elastic-only systems. Relevant specifications of ATLID are given in Table 1. The instrument points 2° off-nadir to avoid detector saturation due to specular reflection from horizontally oriented ice crystals.

The instrument comprises three receiver channels:

– **Mie channel**: Particulate backscattering signal for clouds and aerosols.

https://doi.org/10.5194/egusphere-2026-4436
Preprint. Discussion started: 23 September 2026

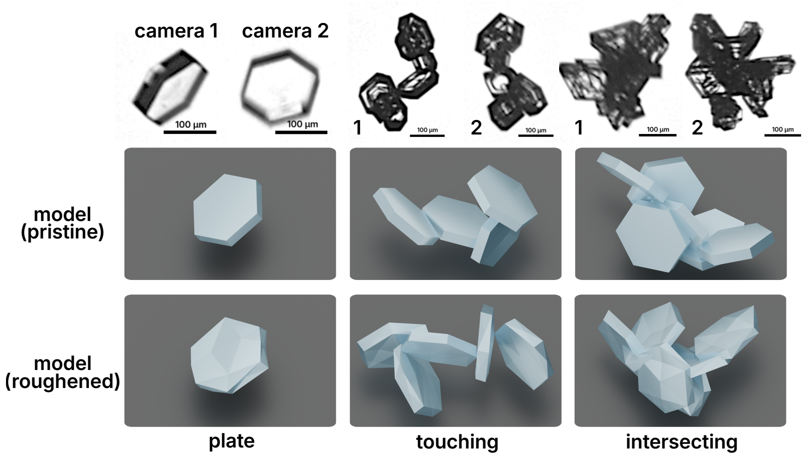

Figure 3. Ice crystal habits observed in-situ and their computational model counterparts. Top row: stereographic camera images from the PHIPS probe showing a single hexagonal plate (left), a touching plate aggregate (centre), and an intersecting plate aggregate (right), each captured from two viewing angles. Middle row: pristine computational geometries used in the physical optics simulations (Sect. 3.2). Bottom row: example geometries of similar size with surface roughness applied ($\sigma_{\%} = 5\,\%$). Columns correspond to the three habits: hexagonal plate, touching aggregate, and intersecting aggregate.

Table 1. ATLID instrument specifications.

Parameter	Value
Wavelength	354.8 nm (UV)
Off-nadir angle	2° (along-track)
Vertical resolution (0–20 km)	∼100 m
Vertical resolution (20–40 km)	500 m
Horizontal resolution (single shot)	∼140 m
Horizontal resolution (L2 products)	1–10 km

– **Rayleigh channel**: Molecular backscatter for atmospheric reference and calibration.

– **Cross-polar channel**: Depolarised backscattering signal for non-spherical particle shape discrimination.

The HSRL principle utilises a high-spectral-resolution Fabry-Pérot etalon to separate the spectrally narrow Mie signal from the Rayleigh signal. From the resulting particulate backscattered signal, the A-PRO (ATLID Profile) processor produces three data products:

– **A-EBD**: Extinction, backscatter, depolarisation.

– **A-TC**: Target classification (e.g., ice cloud, liquid cloud, aerosol).

https://doi.org/10.5194/egusphere-2026-4436
Preprint. Discussion started: 23 September 2026

- **A-ICE**: Ice microphysics (e.g., effective radius, ice water content), derived from an empirical parametrisation using retrieved extinction and temperature (Heymsfield et al., 2014; Donovan et al., 2024).

For this study, ATLID data spanning 24 June to 29 July 2025 (∼35 days) is analysed, temporally matching the CIRRUS-HL summer campaign period from 2021. The CIRRUS-HL data is from summer 2021, while the ATLID data is from summer 2025, introducing a four-year gap between the two datasets. This is mitigated by matching the latitude and temperature ranges (ATLID: $-46\pm13\,°\mathrm{C}$, CIRRUS-HL: $-43\pm9\,°\mathrm{C}$), and by the assumption that ice crystal optical properties depend primarily on habit, size, and roughness rather than the year of observation. Ulanowski et al. (2014) found similar magnitudes of roughness in growth and sublimation zones of cirrus, and only slightly higher roughness in cirrus forming in clean oceanic air masses compared with a continental, polluted one. This provides some justification for comparing in-situ and satellite observations that are seasonally-matched but separated by a 4 year time period.

For global statistics, the low-resolution ($10\,\mathrm{km}$ horizontal) products are chosen to reduce data volume. The datasets are filtered according to the following steps:

1. Input: 41.9 M raw pixel data
2. Ice cloud filter: `classification label = 3` filters out all non-ice-cloud pixels
3. Quality and fill value filter: `quality_status = 3` (good quality only)
4. Longitudinal ($-29.7°$ to $22.0°$), latitudinal (39.3° N to 75.5° N), and height (6.8–$11.3\,\mathrm{km}$) filters, matching CIRRUS-HL flight region
5. Optical depth filter: $0.3 \leq \tau < 1.0$, excluding optically thin clouds where the retrieval suffers from signal noise and optically thick clouds where multiple scattering effects dominate
6. Output: 738 k filtered ice cloud pixels

2.2.1 Ice cloud classification

The ice versus liquid cloud classification is based on temperature and depolarisation ratio, where the linear depolarisation ratio δ is defined as the ratio of cross-polarised to co-polarised backscattered power. Temperature bounds of $T < 0\,°\mathrm{C}$ are used to identify possible ice, while $T < -40\,°\mathrm{C}$ indicates definite ice due to the homogeneous freezing temperature (Irbah et al., 2023). High depolarisation ratio corresponds to non-spherical particles and is used to further constrain the classification. The ratio of integrated depolarisation to backscattering $> 10^{-4}$ is used as the primary ice classifier. The EarthCARE payload uses the synergy between the two active instruments (ATLID and CPR) to identify both large ice particles and thin cirrus (large ice particles with effective radii $>\sim 50\,\mu\mathrm{m}$ detectable by CPR). In practice, temperature is derived from European Centre for Medium-Range Weather Forecasts (ECMWF) operational analysis profiles, depolarisation from ATLID, and empirical thresholds are applied to classify ice clouds. The retrieved lidar and depolarisation ratios for each cloud optical depth category are shown in Fig. 4.

https://doi.org/10.5194/egusphere-2026-4436
Preprint. Discussion started: 23 September 2026

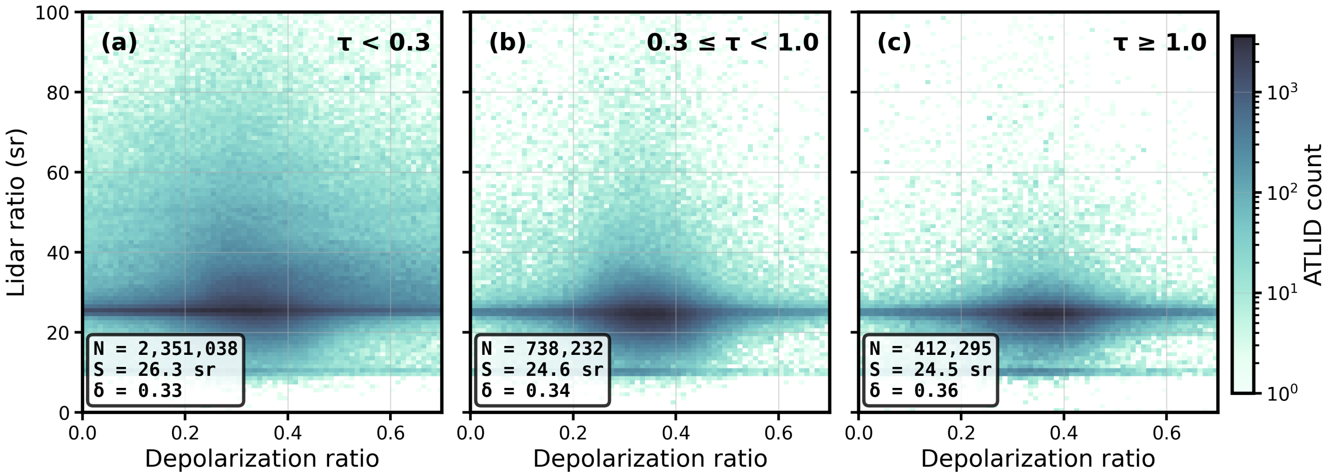

Figure 4. Lidar ratio S versus depolarisation ratio δ for ATLID ice cloud pixels, filtered by cloud optical depth.

2.2.2 Lidar ratio retrieval

The A-EBD framework uses forward-modelling optimal estimation to retrieve total extinction (α), backscatter (β), and thereby the lidar ratio S, defined as α/β (Donovan et al., 2024). The algorithm iteratively adjusts a modelled atmospheric state to best match the observed ATLID signals. A priori values of 25 sr with 20 % uncertainty are used for ice cloud lidar ratio, inherited from Cloud-Aerosol Lidar with Orthogonal Polarization (CALIOP) heritage where 25 sr was the default initial value for cirrus retrievals (Saito et al., 2017). This is a potential source of bias, as retrievals may unfairly tend toward the a priori value when there is insufficient information in the observations. Donovan et al. (2024) state that this can occur for optically thin cirrus when the signal-to-noise ratio limits the constraint on S.

The A-PRO validation scheme used test ice cloud scenes with lidar ratio around 30 sr. The test scenes are based on the Global Environmental Multiscale (GEM) numerical weather prediction (NWP) model (Qu et al., 2023) with ice optics from Baum et al. (2014) assuming aggregated solid columns. The study showed that the A-PRO algorithm can retrieve input lidar ratios around 30 sr, but retrieval of other values was not verified. “Severely roughened” aggregates were used, with optical properties computed using improved geometric optics, representing a specific habit assumption that may not capture the full diversity of ice crystal shapes in nature. Saito et al. (2017) noted that “for cloud optical thickness (COT) inferences over transparent cirrus clouds, 99.7 % of the CALIOP unconstrained retrievals use the initial lidar ratio of 25 sr”. This bias also propagated into the ATLID algorithm development, which can be seen as the horizontal band in Fig. 4. For moderate and optically thick cirrus, the retrieval is fairly well-constrained, retrieving a reasonable spread of physically plausible lidar and depolarisation ratios. For optically thin clouds (see Fig. 4a), the depolarisation ratio appears to be poorly constrained, with ∼13 % of pixels (not shown here) yielding unphysical depolarisation ratios less than 0. Since lidar ratio is proportional to the inverse of the backscattering

https://doi.org/10.5194/egusphere-2026-4436
Preprint. Discussion started: 23 September 2026

cross section, the lack of retrieved lidar ratios with values ≤ 10 indicates that the bulk representative ice particles in cirrus have low backscattering – something usually observed in simulations for roughened or hollow particle geometries.

The ATLID-retrieved lidar ratio and depolarisation ratio as a function of height are shown in Fig. 2e,f. The lidar ratio shows weak variation with height, with median values around 25 sr throughout. Interpretation of lidar ratio must be done with care, since it is clear that the majority of pixels fall directly onto the a-priori estimate of 25 sr. A simple sensitivity test with varying a-priori value would be both of great necessity and utility towards understanding the retrieval confidence. Depolarisation ratio shows a weak increase with height. A cloud chamber study by Hamel et al. (2026) observed an increase in magnitude and variation of depolarisation ratio with decreasing particle size in cold regime (-75 to $-45\,^{\circ}$C). The satellite retrievals are consistent in trend, but the results are not directly comparable because the in-situ particle size measurements (Fig. 2d) are almost an order of magnitude in size larger than those in the cloud chamber. Both studies hint that variation in the lidar and depolarisation ratio can be attributed to a combination of size and geometrical complexity that is naturally a function of temperature and saturation associated with altitude.

3 Simulation

3.1 Physical geometric optics method

Light scattering simulations are performed using the physical geometric optics method described by Ballington and Hesse (2024a), which computes the orientation-averaged Mueller matrix for dielectric polyhedron particle shapes. The method traces beams, applying Fresnel coefficients at each interface, and uses the electromagnetic equivalence theorem to map the resulting near-field to the far-field via a vector surface integral equation. This accounts for the size-dependent nature of the particle scattering problem, including the coherent backscattering enhancement and interference effects that are absent in classical GO. The method is applicable to particles with size parameters exceeding approximately 20, which is acceptable for the size ranges in this study. Simulations are performed at two wavelengths to match the observational instruments: 0.355 µm for comparisons with ATLID lidar and depolarisation ratio retrievals, and 0.532 µm for comparisons with the PHIPS angular scattering measurements. Complex refractive indices for ice from Warren and Brandt (2008) are $n = 1.3249 + 2 \times 10^{-11}i$ at 0.355 µm and $n = 1.3110 + 2.29 \times 10^{-9}i$ at 0.532 µm; in both cases the imaginary part is negligible. During simulation, beams are traced until their cross-sectional area or remaining energy falls below a prescribed threshold. Up to 20 total internal reflections are permitted to allow treatment of multiple scattering paths, and the near-field simulation terminates at 99.9 % energy conservation.

3.2 Particle geometries

As shown in Fig. 2b, plate-like structures constitute the largest classifiable fraction of images in the CIRRUS-HL data ($\sim$30 %) across the sampled altitude range. They are also the dominant particle habits found in convection-driven cirrus cloud formation (Lawson et al., 2019). The particle size distribution for the collated $\sim$12 000 particles is shown in Fig. 5, with peak diameter

https://doi.org/10.5194/egusphere-2026-4436
Preprint. Discussion started: 23 September 2026

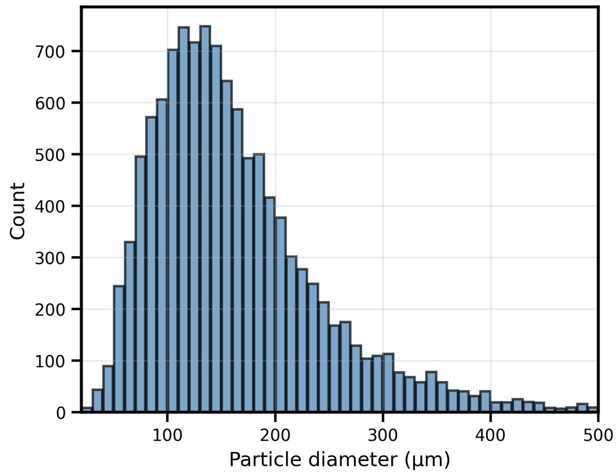

Figure 5. Particle size distribution of the ∼12 000 classified plate, side-plane, and plate aggregate particles measured by PHIPS during CIRRUS-HL.

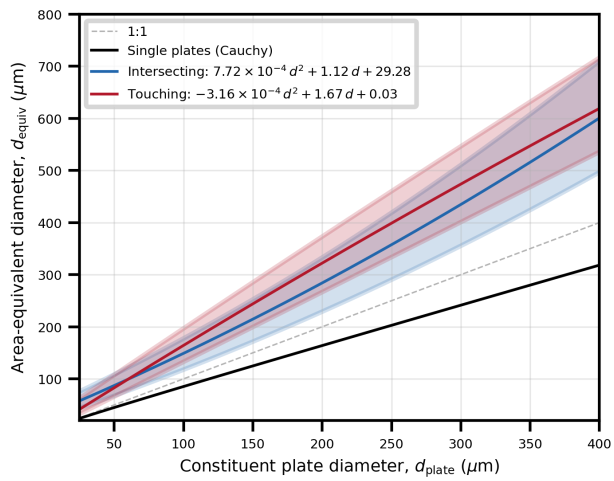

Figure 6. Relationship between constituent plate diameter d_{plate} and area-equivalent diameter d_{equiv} for the three simulated habits. The black curve shows single hexagonal plates (Cauchy's formula), coloured curves show quadratic polynomial fits for intersecting (blue) and touching (red) plate aggregates, with shaded ribbons indicating the 16th–84th percentile spread.

∼128 µm and interquartile range from 107–201 µm, where the diameter is defined as that of a circle with the same projected cross sectional area, taken as a mean of the 2 camera images. The bulk optical scattering as a function of angle and size, along with the detector saturation characteristics, is shown in the supplementary material (Fig. A1).

Three ice crystal habits are simulated: hexagonal plates, touching plate aggregates, and intersecting plate aggregates (Fig. 3, middle and bottom rows). For each habit, an ensemble of 1000 particle geometries is generated with dimensions sampled from

https://doi.org/10.5194/egusphere-2026-4436
Preprint. Discussion started: 23 September 2026

the PHIPS-measured size distributions described in Sect. 2.1 and shown in Fig. 5. Rather than computing scattering properties at a single representative particle size, the computations are performed in a single pass across the measured size distribution, weighted by frequency at each size. This approach provides an additional level of realism to avoid false conclusions arising from size-dependent effects that only occur when a single size is considered.

The particle area-equivalent diameter d_{equiv} is defined as the diameter of a circle with the same orientation-averaged projected area as the particle. For convex bodies such as single hexagonal plates, the orientation-averaged projected area is described by Cauchy's formula as one quarter of the total surface area, from which physical prism dimensions can be derived analytically given a prescribed aspect ratio. For concave bodies such as the plate aggregates, a general closed-form expression does not exist, so d_{equiv} is instead computed numerically using a Monte Carlo ray-casting technique. The particle geometries are described below:

– **Hexagonal Plates:** Plate geometries are hexagonal prisms with dimensions derived from the observed area-equivalent diameters. The PHIPS-measured area-equivalent diameter d_{equiv} is converted to the physical prism diameter d_{phys} via a polynomial fit, and the plate thickness l is computed from the parametrisation of Auer and Veal (1970):

$$l = 2.02\, d^{0.449} \tag{1}$$

where both l and d are in micrometres. The prism circumradius is $r = d/\sqrt{3}$. The resulting ensemble of 1000 plates has a mean diameter of $156 \pm 75\,\mu\text{m}$, consistent with the observed plate population ($156 \pm 85\,\mu\text{m}$).

– **Side-planes and Plate Aggregates:** Side-plane crystals are a polycrystalline form of hexagonal plates, with a formation mechanism observed at temperatures from -20 to $-40\,^{\circ}\text{C}$ with 20–60 % ice supersaturation (Bailey and Hallett, 2009). They can be represented in numerical simulation by conjoined single plates. Each aggregate is constructed here as a sequential assembly of a random number (uniformly distributed between 2 and 8) of identical hexagonal plates. The constituent plate diameter is determined by inverting the observed PHIPS aggregate diameter: a forward lookup table is first constructed by generating many random aggregate realisations for a range of plate diameters and computing the resulting area-equivalent diameter in each case. The mean ratio of aggregate diameter to plate diameter provides a scaling factor, and for each observed aggregate the constituent plate diameter is recovered by dividing by this factor. Each plate is assigned a random orientation (uniformly distributed on SO(3)) and then positioned relative to the growing aggregate using a binary search along the vertical axis. Two morphological variants are considered:

  – ***Touching:*** Each new plate is lowered until it just contacts the aggregate surface without overlap, producing loosely packed structures. This structure is a geometrical representation of a plate aggregate.

  – ***Intersecting:*** Each new plate is lowered until partial volumetric overlap is detected, and the geometry is merged via boolean union, producing more compact aggregates, which resemble side-plane geometries.

For each morphological variant, an ensemble of 1000 aggregates is generated whose area-equivalent diameters are consistent with the observed side-plane population. This stochastic assembly approach, sampling the number of constituent plates, their orientations, and their attachment positions from random distributions constrained by the observed size distribution, produces a diverse ensemble of random polycrystalline geometries.

Surface roughness is applied to the pristine geometries using a mesh refinement and displacement procedure (Ballington and Hesse, 2024b). Each pristine geometry is first refined using MMG surface remeshing (Dapogny et al., 2014) to increase the mesh resolution, and then each vertex is displaced along its surface normal by a random amount drawn from a uniform distribution $\mathcal{U}(-\sigma,+\sigma)$, where σ is proportional to the particle diameter:

$$\sigma = \frac{\sigma_{\%}}{100} \times d_{\text{phys}} \tag{2}$$

For side-plane aggregates, each constituent plate is roughened individually before joining, meaning that the displacement magnitude is relative to the monomer plate size. Twenty-one roughness levels are simulated, from 0 % (pristine) to 10 % in 0.5 % increments. Because the roughness implementation creates physical, 3D geometry realisations, at higher roughnesses the meshes can self-intersect and in such cases the meshes are rejected. At 10 % roughness, the number of valid meshes is approximately 65 %.

For each ensemble, the model computes the orientation-averaged Mueller matrix. For plates, 10^6 uniformly distributed orientations are used per ensemble; for side-plane aggregates, 2.5×10^5 orientations are used. The lidar and linear depolarisation ratio are extracted from the 4×4 Mueller matrix at the backscatter direction ($\theta = 180°$). Full details are given in Appendix A.

4 Results and discussion

4.1 Angular scattering profile

Fig. 7 shows the variation in angular scattering intensity measured by the PHIPS instrument. The data is filtered to a size range 100–150 µm, which encompasses the peak of the measured size distribution. The measurement is calibrated to account for manufacturer-prescribed photomultiplier tube non-uniformity (Appendix B). While the grey band shows significant variation in angular scattering profiles on a per-particle basis, the variation between the means of each habit is small and almost within measurement uncertainty. The results suggest that a single representative model may be sufficient for constraining S_{11} across the measured angular range. Fig. 8 shows the simulated Mueller matrix elements for the 30–60 µm size bin, with the S_{11} element compared against PHIPS in-situ measurements. The smaller size bin is used here since the measurement is less susceptible to saturated detector channels (Fig. A1. Both the touching and the single plates in the smooth case show more structure than the others. For example, the halo peak is present, evidenced by a flattening in the scattering at 18°, and a small, broad peak at 46° can be seen. The most discriminating feature in the measured pattern is the first measurement point, where simulated S_{11} for pristine plates and smooth touching aggregates are outside the measurement uncertainty. No clear case can be made for a suitable choice of representative habit among the other geometries investigated. More discerning features, especially for discrimination between smooth intersecting aggregates and the roughened geometries, can be seen in the polarisation elements. Interestingly, despite the single plate and touching plate aggregate habits showing close resemblance in their angular scattering

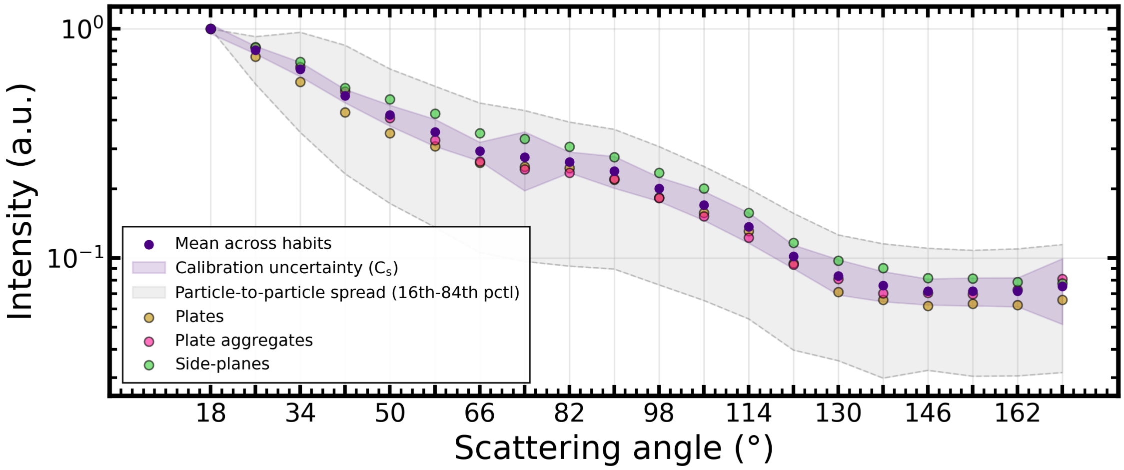

Figure 7. Habit-resolved angular scattering measured by the PHIPS probe during CIRRUS-HL, filtered to the peak 100–150 μm size bin. Coloured markers show the mean normalised intensity for each habit class (mustard: single plates; pink: plate aggregates; green: side-planes). Purple markers show the mean across the three habit classes (single plates, plate aggregates, side-planes), and the purple band is the channel-to-channel calibration uncertainty C_s, defined as the relative standard deviation of each detector channel derived from the instrument reference calibration. The grey band shows the particle-to-particle spread (16th–84th percentile) in each bin. Per-habit statistical uncertainty is not shown because it is smaller than the marker size at almost all angles.

profiles, their asymmetry parameter g values vary significantly. The computed g values are 0.872 (**0.860**), 0.869 (**0.837**), and 0.849 (**0.843**) for single plates, intersecting aggregates, and touching aggregates respectively, with 5% roughness values given in parentheses. Based on the lack of variation between the investigated rough particle geometries, a single representative habit may be a suitable for optical characterisation, although whether or not a single habit can describe all the matrix elements requires more polarimetric observational data for comparison.

4.2 Lidar ratio and depolarisation ratio

In Fig. 9a, the observed lidar ratio and depolarisation ratio measurement pairs show the spread of possible scattering that could be attributed to cirrus cloud. Simulated backscattering properties are shown as scatter points, and each simulation is a bulk calculation averaged over the particle size distribution (Fig. 5). S–δ parametric splines as a function of surface roughness are shown as solid lines. The lines are fixed to start at the pristine smooth variants of each model. Due to the fairly complex particle geometry, it is accepted that a considerable amount of the coherent backscattering enhancement (associated with edge and corner diffraction effects) cannot be accounted for by the PO model. Therefore, it is possible that the backscattering cross section is underestimated by a factor ~ 1.5. The uncertainty is low-biased, which translates to a high-bias in the simulated S value. Fig. 9a acknowledges this by representing the uncertainty as coloured bands below each parametric spline fit. All pristine versions of the different models have similar (S, δ) values, with depolarisation ratio between 0.2 and 0.3 and the

https://doi.org/10.5194/egusphere-2026-4436
Preprint. Discussion started: 23 September 2026

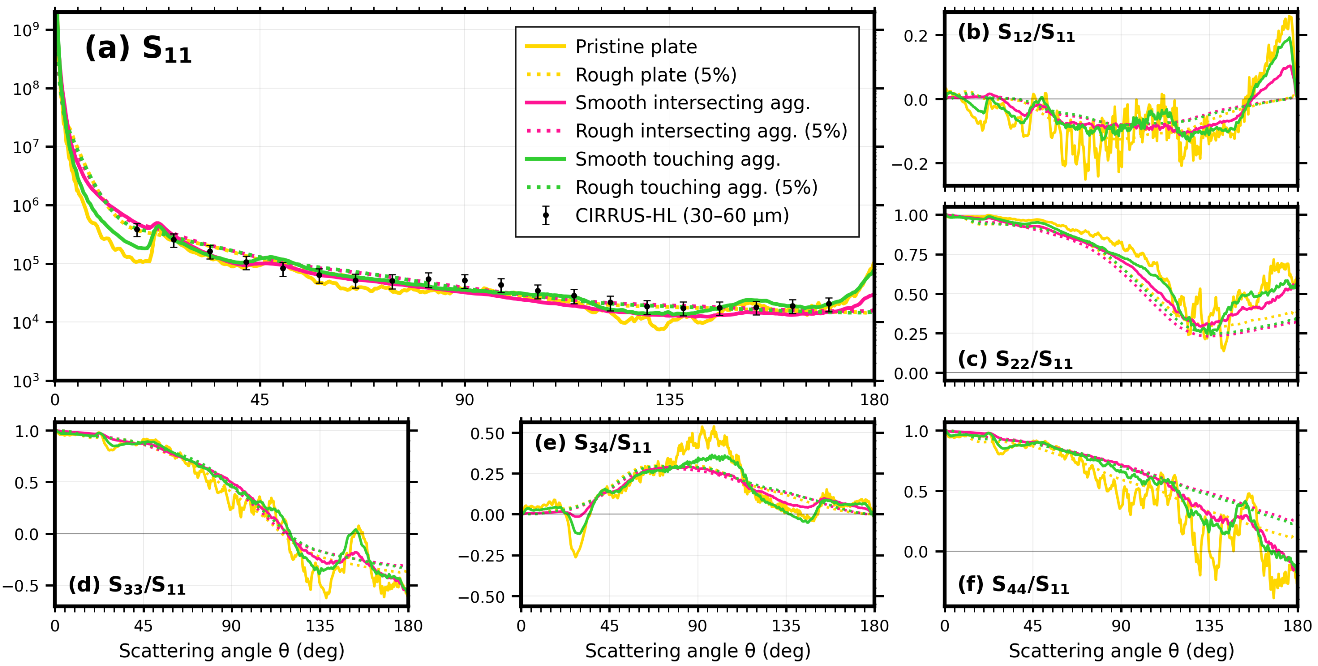

Figure 8. Simulated Mueller matrix elements for the 30–60 µm size bin. (a) S_{11} compared with PHIPS in-situ measurements from CIRRUS-HL (black markers). Solid lines show smooth (0 % roughness) habits; dotted lines show the corresponding 5 % roughened variants. Colours indicate habit: yellow for hexagonal plates, pink for intersecting aggregates, green for touching aggregates. The PHIPS data are normalised so that the area under the curve from 18–170° matches the mean simulated area. Error bars combine the standard error of the mean with a 25 % systematic uncertainty added in quadrature. (b–f) Normalised Mueller matrix elements S_{12}/S_{11}, S_{22}/S_{11}, S_{33}/S_{11}, S_{34}/S_{11}, and S_{44}/S_{11} for the same variants (no in-situ comparison available).

lidar ratio around the modal value of the retrieved observed ratios; touching plate aggregates remain near the modal value across all simulated roughness levels. Quantifying this in terms of the log-Euclidean residual to the observed mode at $(S,\delta) = (24.5\,\mathrm{sr}, 0.345)$, pristine plates ($\epsilon = 0.12$), pristine intersecting aggregates ($\epsilon = 0.17$) and all touching variants (smooth $\epsilon = 0.39$, 5 % $\epsilon = 0.39$, 10 % $\epsilon = 0.45$) all sit within $\epsilon < 0.5$, while roughened plates and roughened intersecting aggregates lie further out at $\epsilon > 1$. Fig. 9b shows the S–δ distribution of the observed cirrus overlaid with single-scattering values from existing habit databases taken from the literature. Reassuringly, the smooth intersecting plate aggregate simulated here ($S = 22.4\,\mathrm{sr}$, $\delta = 0.230$) agrees closely with the cluster of smooth plate aggregate values from the Yang et al. (2013) database in the high-density region of the retrieval ($S = 24.5 \pm 1\,\mathrm{sr}$, $\delta = 0.235 \pm 0.01$), with the lidar ratio and depolarisation ratio agreeing to within 9 % and 3 % respectively.

The behaviour of lidar ratio and depolarisation ratio with increasing roughness varies depending on the habit. Single plates show the strongest dependence, with roughness giving a sharp increase in lidar ratio. This can be attributed to a sharp decrease in the backscattering cross section, since it is well known that pristine plates exhibit a strong backscattering, which is diminished

https://doi.org/10.5194/egusphere-2026-4436
Preprint. Discussion started: 23 September 2026

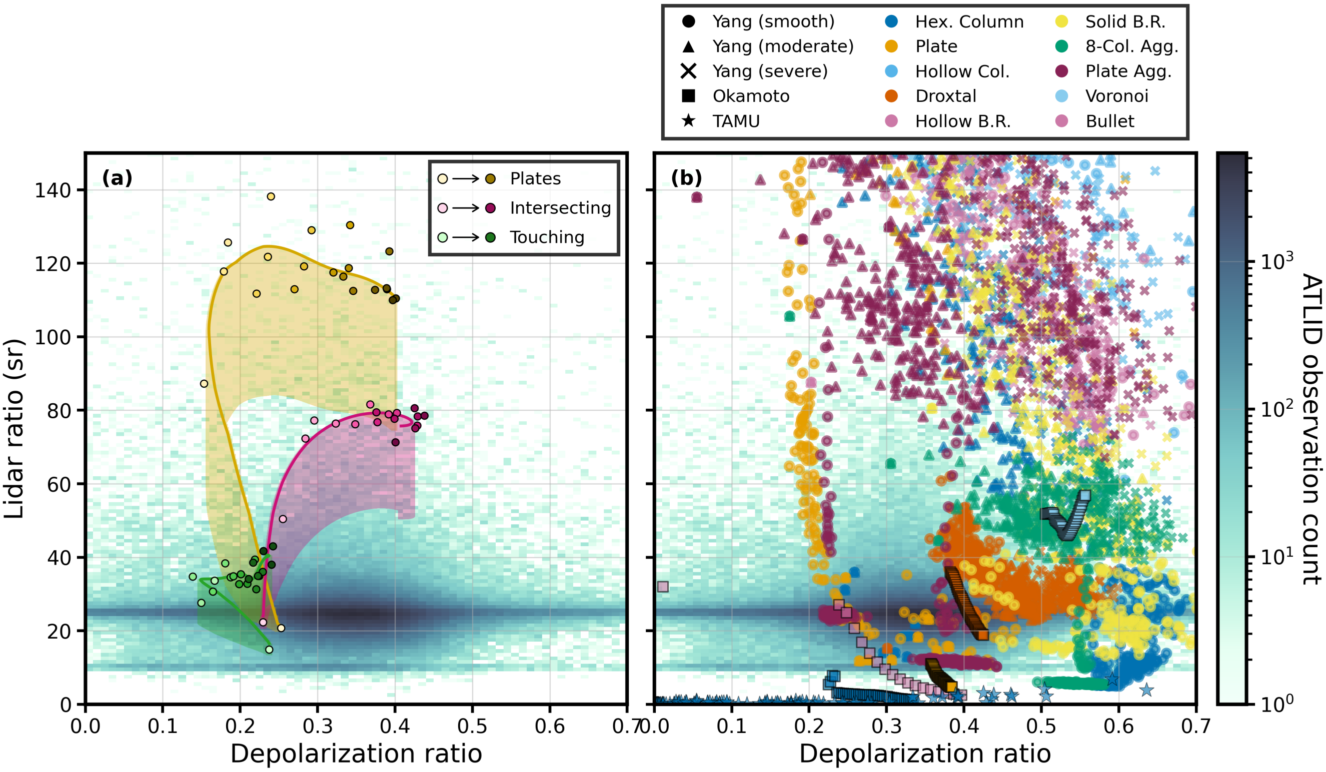

Figure 9. ATLID-retrieved lidar ratio and depolarisation ratio compared with simulations from this study and existing literature databases. (a) Lidar ratio S versus depolarisation ratio δ from ATLID observations of cirrus clouds filtered to optical depths $0.3 \leq \tau < 1.0$. Coloured lines show the simulated bulk scattering properties from the physical geometric optics simulations of this study, with increasing surface roughness indicated by darkening marker colour, from 0 % (start of each line) to 10 %. Shaded bands indicate the uncertainty in the simulation arising from the under-representation of the backscattering cross section. (b) Same ATLID S–δ retrieval overlaid with simulated single-scattering values from existing literature. Circles, triangles, and crosses denote the smooth, moderately roughened, and severely roughened ice crystal models from the Yang et al. (2013) database, respectively, while squares show the three-dimensional randomly oriented results from Okamoto et al. (2020). Different colours indicate different ice crystal habits. Bullet rosettes are abbreviated as "B. R.".

in the presence of roughness. For intersecting and touching plates, the effect of roughness is somewhat less severe owing to the pre-existing shape complexity. It is thought that the behaviour is a competition between two different effects. In analogy to the single plates, roughness decreases the specular or retroreflection peak associated with the pristine hexagonal column geometry. Secondly, the increased macroscopic shape complexity (larger number of facets leads to more scattering) leads to more scattering events in the near-field. In the PO framework, this creates a greater number of narrower beams, which lead to diffuse scattering when mapped to the far-field with Fraunhofer diffraction theory. For a single plate, the light has only a few different paths that it can take in order to scatter into the backscattering direction. Introducing roughness essentially removes those possible paths, decreasing backscattering cross section and thereby increasing lidar ratio. For the touching or

https://doi.org/10.5194/egusphere-2026-4436
Preprint. Discussion started: 23 September 2026

intersecting aggregate, when roughness is introduced, because the diffuse scattering already contributes to a large fraction of the backscattering, the effect of roughness is diminished. This means that for the intersecting particle, the change in lidar ratio due to the presence of roughness is smaller than that of the single plate, and the effect is weaker still for the touching plate aggregate.

There is some trend across all three different habits in terms of depolarisation ratio. A small amount of roughness decreases the depolarisation ratio, and then as roughness increases further, that effect is reversed, with an increasing depolarisation ratio spread across a range from 0.1 to about 0.5. Independent of habit, roughness generally increases depolarisation ratio, aligning with rigorous simulations by Saito and Yang (2023), but the exact form of how roughness affects δ appears to be a function of both habit and particle size. In terms of where the simulated points lie relative to the observations, severely roughened plates, and to some extent severely roughened intersecting plates, fall outside the high-density region of the retrieved S–δ distribution. Because the bulk lidar ratio is dominated by particles with the largest backscattering cross section (Sect. 4.4), this does not necessarily imply that these habits are absent from the cloud. Rather, it indicates that they are not the dominant contributors to the backscattering signal. A cloud composed predominantly of severely roughened plates would produce a bulk lidar ratio inconsistent with the observations, but these particles could still be present as a minority population without significantly affecting the measured S–δ values.

Combining the PHIPS phase function comparison with the ATLID S–δ observations narrows the candidates. This study concludes that smooth intersecting aggregate and roughened touching aggregate have single-particle S–δ values that best overlap with the high-density region of the ATLID retrievals. This means that a cloud in which these habits are the dominant backscatterers would reproduce the observed S–δ distribution. However, it does not exclude other habits from being present in the cloud, provided their backscattering cross sections are weak in comparison so that they do not influence the bulk lidar ratio. Polarimetric in-situ measurements would be valuable here for understanding how the bulk backscatter depolarisation can be related, if at all, to depolarisation at a single particle scale.

4.3 Comparison with previous observations

Satellite observations from the CALIOP instrument show a dense population of measurements with lidar ratio from 10 to 45 sr and depolarisation ratio from 0.3 to 0.6 (Saito and Yang, 2023). Saito and Yang found that hexagonal columns with moderate roughness ($\sigma^2 = 0.03$–0.15) tend to fall within this range, and that scanning electron microscope measurements of ice crystal surface roughness by Butterfield et al. (2017) and Neshyba et al. (2013) also aligned with this scale of roughness. Saito and Yang also concluded that some degree of surface roughness must be present if droxtal particles exist in the cloud, and that this is presumably a one-way process in the growth-sublimation cycle (Voigtländer et al., 2018). They showed that growth-sublimation cycles lead to a net increase in surface roughness, with longer-lived crystals becoming increasingly complex in both their macroscopic shape and surface texture. The increase in roughness during a growth phase was not mirrored by an equal decrease during the subsequent sublimation phase, resulting in a gradual “ratcheting-up” of roughness; a process driven by relative humidity oscillations that is not yet well represented in models. Furthermore, Schnaiter et al. (2016) showed in

https://doi.org/10.5194/egusphere-2026-4436
Preprint. Discussion started: 23 September 2026

cloud chamber simulation experiments on cirrus ice crystal growth under defined supersaturation ratios that optically effective crystal surface roughness already starts to form at rather low ice supersaturation ratios of about 5%.

The CIRRUS-HL PHIPS data is filtered to plates and polyplate habits, whereas the ATLID lidar ratio and depolarisation ratio represent the bulk backscatter-weighted scattering properties across all habits present in the resolution volume. The ATLID S–δ comparison therefore constrains which habits are compatible as dominant backscatterers, but does not provide information about the composition of the cloud as a whole. In mid-latitude cirrus, plate-based geometries are known to be abundant due to the humidity and available water content, which lends plausibility to the interpretation that these habits dominate the backscattering signal.

4.4 Backscatter weighting and interpretive limits

The lidar ratio is a backscatter-weighted quantity (Eq. (A10)). Particles with large backscattering cross section dominate the denominator and therefore dominate the signal measured by the lidar instrument. For example, pixels contaminated by sun glint are excluded from the ATLID retrieval because specular reflection from oriented plates and columns can overwhelm the backscatter signal. This means that the lidar ratio is well suited for retrieving the extinction coefficient within the cloud, since the ratio directly converts the measured backscatter into extinction. However, for identification of specific particle habits from the retrieved lidar ratio, the measurement is biased towards the habits and orientations with the strongest backscatter and does not necessarily represent the bulk particle population.

To illustrate the magnitude of this effect, consider a 50/50 mixture of two habits with equal extinction cross sections but lidar ratios of 10 sr and 100 sr, respectively. The low-S habit has 10 times the backscattering cross section, so it dominates the denominator. The resulting bulk lidar ratio is $S_{\text{bulk}} = 2C_{\text{ext}}/(C_{\text{ext}}/10 + C_{\text{ext}}/100) \approx 18\,\text{sr}$, much closer to the strongly backscattering habit. Even at only 10 % fraction, the low-S habit would decrease the bulk lidar ratio from 100 sr down to ∼53 sr. This means that comparing single-particle simulations against the ATLID S–δ distribution primarily constrains which habits dominate the backscattering signal, with limited sensitivity to weakly backscattering populations.

In particular, particles that contribute significantly to extinction but produce weak backscatter (certain orientations of smooth plates) are heavily down-weighted in the lidar signal relative to their contribution to the total extinction. The retrieved bulk lidar ratio accounts for the extinction from all particles, since the retrieval algorithm constrains S using both the backscatter signal and the observed two-way attenuation caused by the entire particle population. However, the retrieved lidar ratio cannot be straightforwardly mapped to specific particle habits, since the same bulk S value can arise from different combinations of strongly and weakly backscattering particles.

While the JAXA Level 2 cloud products for EarthCARE operationally classify ice habits based on S–δ diagrams (Sato et al., 2025), the present study demonstrates that the backscatter-weighted nature of the lidar ratio introduces a degeneracy: different mixtures of habits and roughness levels can produce indistinguishable bulk (S, δ) values, limiting the ability to infer habit composition from these two parameters alone. It may be worth noting that van Diedenhoven (2018) warns “interpretations of lidar depolarisations in ice clouds are more qualitative than quantitative” and that systematic variations remain “inconclusive” with respect to habit identification. van Diedenhoven argues that it is practically impossible to consider all ice crystal geometries

https://doi.org/10.5194/egusphere-2026-4436
Preprint. Discussion started: 23 September 2026

formed in natural clouds, that any inferred shape should be interpreted as a radiative-equivalent effective shape rather than a direct identification of the habit population, and that for remote sensing it may be more productive to focus on continuous shape parameters such as component aspect ratios and microscale roughness, rather than on discrete habit classification.

5 Conclusions

This study combines observational data from two campaigns and two instruments: the satellite-based ATLID high-spectral-resolution lidar aboard the EarthCARE mission, and the PHIPS in-situ nephelometer probe during the CIRRUS-HL campaign. The analysed data spans a mid-latitude range from 39.3–75.5° N and longitude from −29.7 to 22.0° (Fig. 1), covering a region over the Arctic, North Atlantic, Central Europe, Scandinavia, and Iceland. The temperature range of the satellite data is $-46 \pm 13\,°\mathrm{C}$, overlapping with the in-situ range of $-43 \pm 9\,°\mathrm{C}$.

The unfiltered satellite data comprises ∼42 million raw pixel data points, and is then filtered by ice cloud classification, quality control, geographic matching, and cloud optical depth ($0.3 \leq \tau < 1.0$) to yield 738 000 ice cloud pixels from which the retrieved backscattered intensity and polarisation state are investigated. The equivalent PHIPS data from the HALO aircraft is collated across 22 flights from 24 June to 29 July 2021, whereas the ATLID observational data is from 2025. The in-situ measurements capture both the angular scattering pattern from 18–170° and simultaneously acquire stereographic images of the ice particles from two orientations. The resulting dataset comprises approximately 12 000 manually classified plate, side-plane, and plate aggregate particles, with a size distribution peaking at approximately 128 µm and an interquartile range from 107–201 µm (Fig. 5).

Together, the two campaigns provide complementary perspectives on the cloud: the bulk backscatter-weighted lidar ratio S (Eq. (A10)) and depolarisation ratio δ retrieved from ATLID, and the angular scattering of individual particles along with real particle size distributions for classified plates and aggregates of plates from PHIPS. Since the backscattering properties of compact hexagonal columns have already been investigated by Saito and Yang (2023), this study chose to focus on hexagonal plates and habits derived from the base hexagonal plate geometry, referred to here as side-plane aggregates. It is frequently observed in nature that fewer than 10 % of ice particles are typically classifiable as idealised pristine habits (Lawson et al., 2019; Korolev et al., 1999); instead, aggregates and irregular shapes dominate. This study therefore constructs two computational models for representing aggregates: touching plate aggregates, where each new plate contacts the existing aggregate surface without overlap, and intersecting plate aggregates, where the plates are partially overlapped and joined via a geometric boolean union, yielding more compact structures.

A physical geometric optics method (Ballington and Hesse, 2024a) is used to simulate the orientation-averaged scattering properties for each habit. In addition, surface roughness is applied in increments from 0 to 10 % of the monomer plate diameter, and the effect on the bulk scattering properties is investigated. For each habit and roughness level, an ensemble of 1000 particles with sizes sampled from the measured distribution is generated, and both the backscattering properties relevant to lidar and the differential scattering cross section measured by PHIPS are computed as orientation and ensemble averages.

https://doi.org/10.5194/egusphere-2026-4436
Preprint. Discussion started: 23 September 2026

The PHIPS phase function comparison (Fig. 8a) is consistent with simulated smooth intersecting aggregate models, as well as all roughened models, but there is insufficient evidence for further constraint from S_{11} alone. The combination of PHIPS and ATLID data narrows the candidates: smooth intersecting aggregates and the roughened touching aggregate are the habits whose single-particle S–δ values best overlap with the high-density region of the ATLID retrievals, while simultaneously showing reasonable agreement with the measured PHIPS phase function. In terms of a single-habit representation, these are the best candidates for computational models of the dominant backscatterers in the observed cirrus. It is emphasised that the bulk cloud is composed of a mixture of different habits, and one can arrive at similar bulk S–δ values with a multitude of different habit mixtures. The lidar ratio constrains which habits dominate the backscattering signal, but does not uniquely determine the composition of the cloud as a whole.

Fig. 9a shows the simulated lidar ratio and depolarisation ratio for each habit overlaid on the ATLID retrieval data. The pristine smooth versions of all three habits lie within the range of the retrieved observational data. However, any degree of surface roughening on single plates leads to lidar ratios far exceeding those measured by ATLID, suggesting that while roughened plates may be present in the cloud, they only weakly contribute to the retrieved backscatter signal. This is because pristine plates have strong retroreflection-driven backscattering, and roughness destroys those specular paths, drastically reducing the backscattering cross section. Similarly, for the intersecting aggregates, the data spreads into the observed range but remains concentrated around the smooth variants. Since the bulk lidar ratio is heavily weighted by particles with large backscattering cross sections (Sect. 4.4), these smooth pristine habits naturally dominate the retrieved signal. In contrast, the touching aggregates in all variants of roughness lie within a reasonable spread of the observed data, with depolarisation ratio from 0.1 to 0.3 and lidar ratio from approximately 25 to 45 sr. It is thought that this can be attributed to the complex overall shape of the touching aggregates, which increases the backscattering contribution due to diffuse scattering; roughness therefore has a diminished effect on the backscattering cross section compared to the single plate case.

In summary, this study presents a promising new avenue for combining satellite-based HSRL retrievals from EarthCARE with in-situ single-particle scattering and imaging, together with state-of-the-art physical optics simulations of plate and aggregate geometries with varying surface roughness. The results provide an up-to-date assessment of our understanding and interpretation of lidar data and in-situ measured scattering in mid-latitude cirrus, and highlight the key areas, particularly the need for more realistic particle geometries and better-constrained roughness parameterisations, that must be addressed to improve the representation of ice cloud radiative properties in future retrieval and climate modelling frameworks. While in-situ and remote sensing measurements provide complementary information for constraining cirrus cloud optical properties, future studies would greatly benefit from in-situ polarimetric measurements in order to fully understand the intricacies of satellite retrievals.

Appendix A: Lidar ratio derivation from Mueller matrix output

The lidar ratio S is defined as the ratio of extinction cross section to backscatter cross section:

$$S = \frac{\langle C_{\text{ext}} \rangle}{\langle C_b \rangle} \tag{A1}$$

https://doi.org/10.5194/egusphere-2026-4436
Preprint. Discussion started: 23 September 2026

where angle brackets denote orientation averaging. To compute S from the model output, we must relate the Mueller matrix elements to the backscatter cross section.

Following Mishchenko et al. (1999), the orientation-averaged backscatter cross section is:

$$\langle C_b \rangle = \frac{\langle C_{\text{sca}} \rangle \, a_1(180°)}{4\pi} \tag{A2}$$

where $a_1(\theta)$ is the $(1,1)$ element of the normalised scattering matrix, with normalisation:

$$\frac{1}{2}\int_0^{\pi} a_1(\theta) \sin\theta \, d\theta = 1 \tag{A3}$$

The model outputs the Mueller matrix element S_{11} in either 2D form (as a function of θ and ϕ) or 1D form (integrated over azimuth). The total scattering cross section is recovered from the 2D output as:

$$C_{\text{sca}} = \frac{1}{k^2}\int_0^{2\pi} d\phi \int_0^{\pi} S_{11}^{(\text{2D})}(\theta,\phi) \sin\theta \, d\theta \tag{A4}$$

where $k = 2\pi/\lambda$ is the wavenumber. The 1D Mueller matrix is the azimuthal integral of the 2D form:

$$S_{11}^{(\text{1D})}(\theta) = \int_0^{2\pi} S_{11}^{(\text{2D})}(\theta,\phi) \, d\phi \tag{A5}$$

Substituting Eq. (A5) into Eq. (A4) gives the scattering cross section in terms of the 1D output:

$$C_{\text{sca}} = \frac{1}{k^2}\int_0^{\pi} S_{11}^{(\text{1D})}(\theta) \sin\theta \, d\theta \tag{A6}$$

Combining Eq. (A6) with the Mishchenko normalisation Eq. (A3) and equating integrands yields the relation between the 1D output and the normalised phase function:

$$S_{11}^{(\text{1D})}(\theta) = \frac{C_{\text{sca}} k^2}{2} a_1(\theta) \tag{A7}$$

Evaluating at the backscatter direction ($\theta = 180°$) and substituting into the expression for $\langle C_b \rangle$ Eq. (A2):

$$\langle C_b \rangle = \frac{C_{\text{sca}}}{4\pi} \cdot \frac{2\, S_{11}^{(\text{1D})}(180°)}{C_{\text{sca}} k^2} = \frac{S_{11}^{(\text{1D})}(180°)}{2\pi k^2} \tag{A8}$$

For randomly oriented particles, the scattering matrix is azimuthally symmetric, so $S_{11}^{(\text{1D})}(180°) = 2\pi \, S_{11}^{(\text{2D})}(180°)$ and equivalently:

$$\langle C_b \rangle = \frac{S_{11}^{(\text{2D})}(180°)}{k^2} \tag{A9}$$

The lidar ratio then follows directly:

$$S = \frac{\langle C_{\text{ext}} \rangle}{\langle C_b \rangle} = \frac{2\pi k^2 \langle C_{\text{ext}} \rangle}{S_{11}^{(\text{1D})}(180°)} = \frac{k^2 \langle C_{\text{ext}} \rangle}{S_{11}^{(\text{2D})}(180°)} \tag{A10}$$

In practice, the model reports $\langle C_{\text{ext}} \rangle$ directly from energy conservation (incident minus scattered plus absorbed), so the lidar ratio is computed from the extinction cross section and the backscatter Mueller matrix element.

https://doi.org/10.5194/egusphere-2026-4436
Preprint. Discussion started: 23 September 2026

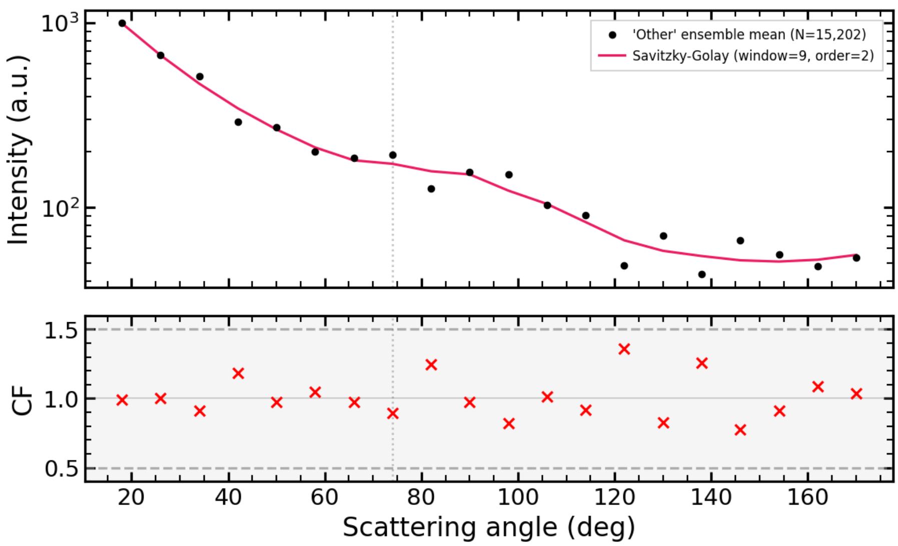

Figure B1. Channel calibration factor diagnostic plot.

Appendix B: Photomultiplier Tube Non-Uniformity Correction

Each detector channel in the PHIPS instrument has a photomultiplier tube with a channel-to-channel manufacturer-prescribed
545 non-uniformity of 50%. To correct for this, the measured campaign data is filtered to $\sim 15,000$ particles from the "Other" habit category. Since features in the scattering pattern arise from symmetries and large, smooth surfaces, it is reasonably safe to assume that particles from this habit should have smooth, featureless phase functions. Based on this, a stride-9 Savitzky-Golay filter is fitted to the data, which yields an estimated correction factor (CF) for each scattering channel. The results are shown in Fig. B1. As expected, all correction factors lie within the manufacturer-prescribed bounds.

550 *Author contributions.* HB conceived the study, developed the simulation framework, performed the physical optics computations, processed and analysed the ATLID and PHIPS data, and wrote the manuscript. MS provided the PHIPS instrument and data, contributed to the data analysis and interpretation, and reviewed the manuscript. EJ supervised the study, contributed to the scientific interpretation, and reviewed the manuscript.

Competing interests. The authors declare that they have no conflict of interest.

https://doi.org/10.5194/egusphere-2026-4436
Preprint. Discussion started: 23 September 2026

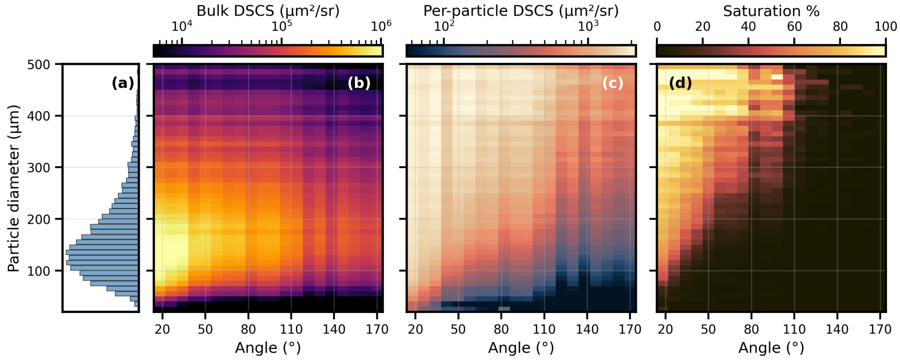

Figure A1. PHIPS bulk scattering and detector saturation for plate and side-plane particles. (a) Particle size distribution. (b) Bulk scattering contribution per size bin, computed as the sum of calibrated scattering values with saturated channels replaced by the detector ceiling. (c) Per-particle mean scattering, obtained by dividing panel (b) by the particle count in each bin. (d) Percentage of saturated detector channels at each particle size and scattering angle, showing increased saturation for larger particles and forward scattering angles.

Acknowledgements. The authors acknowledge the use of EarthCARE ATLID data products provided by ESA and JAXA. The CIRRUS-HL campaign was supported by the German Research Foundation (DFG).

References

Auer, A. H. and Veal, D. L.: The Dimension of Ice Crystals in Natural Clouds, Journal of the Atmospheric Sciences, 27, 919–926, https://doi.org/10.1175/1520-0469(1970)027<0919:TDOICI>2.0.CO;2, 1970.

Auriol, F., Gayet, J.-F., Febvre, G., Jourdan, O., Labonnote, L., and Brogniez, G.: In Situ Observation of Cirrus Scattering Phase Functions with 22° and 46° Halos: Cloud Field Study on 19 February 1998, Journal of the Atmospheric Sciences, 58, 3376 – 3390, https://doi.org/10.1175/1520-0469(2001)058<3376:ISOOCS>2.0.CO;2, 2001.

Bailey, M. P. and Hallett, J.: A Comprehensive Habit Diagram for Atmospheric Ice Crystals: Confirmation from the Laboratory, AIRS II, and Other Field Studies, Journal of the Atmospheric Sciences, 66, 2888–2899, https://doi.org/10.1175/2009JAS2883.1, 2009.

Ballington, H. and Hesse, E.: A light scattering model for large particles with surface roughness, Journal of Quantitative Spectroscopy and Radiative Transfer, 323, 109 054, https://doi.org/https://doi.org/10.1016/j.jqsrt.2024.109054, 2024a.

Ballington, H. and Hesse, E.: Numerical Simulation of the Effects of Surface Roughness on Light Scattering by Hexagonal Ice Plates, Atmosphere, 15, https://doi.org/10.3390/atmos15091051, 2024b.

Baran, A. J.: A review of the light scattering properties of cirrus, Journal of Quantitative Spectroscopy and Radiative Transfer, 110, 1239–1260, https://doi.org/https://doi.org/10.1016/j.jqsrt.2009.02.026, xI Conference on Electromagnetic and Light Scattering by Non-Spherical Particles: 2008, 2009.

Baran, A. J.: From the single-scattering properties of ice crystals to climate prediction: A way forward, Atmospheric Research, 112, 45–69, https://doi.org/https://doi.org/10.1016/j.atmosres.2012.04.010, 2012.

Baum, B. A., Yang, P., Heymsfield, A. J., Schmitt, C. G., Xie, Y., Bansemer, A., Hu, Y.-X., and Zhang, Z.: Improvements in Shortwave Bulk Scattering and Absorption Models for the Remote Sensing of Ice Clouds, Journal of Applied Meteorology and Climatology, 50, 1037–1056, https://doi.org/10.1175/2010JAMC2608.1, 2011.

Baum, B. A., Yang, P., Heymsfield, A. J., Bansemer, A., Cole, B. H., Merrelli, A., Schmitt, C., and Wang, C.: Ice cloud single-scattering property models with the full phase matrix at wavelengths from 0.2 to 100 µm, Journal of Quantitative Spectroscopy and Radiative Transfer, 146, 123–139, https://doi.org/10.1016/j.jqsrt.2014.02.029, 2014.

Bi, L., Yang, P., Kattawar, G. W., Hu, Y., and Baum, B. A.: Diffraction and external reflection by dielectric faceted particles, Journal of Quantitative Spectroscopy and Radiative Transfer, 112, 163–173, https://doi.org/https://doi.org/10.1016/j.jqsrt.2010.02.007, international Symposium on Atmospheric Light Scattering and Remote Sensing (ISALSaRS'09), 2011.

Borovoi, A., Konoshonkin, A., and Kustova, N.: Backscatter ratios for arbitrary oriented hexagonal ice crystals of cirrus clouds, Optics Letters, 39, 5788–5791, https://doi.org/10.1364/OL.39.005788, 2014.

Borovoi, A., Konoshonkin, A., and Kustova, N.: Coherent and incoherent backscattering by a single large particle of irregular shape, Optics Express, 27, 32 984–32 993, https://doi.org/10.1364/OE.27.032984, 2019.

Borovoi, A. G. and Grishin, I. A.: Scattering matrices for large ice crystal particles, J. Opt. Soc. Am. A, 20, 2071–2080, https://doi.org/10.1364/JOSAA.20.002071, 2003.

Burkhardt, U. and Kärcher, B.: Global radiative forcing from contrail cirrus, Nature Climate Change, 1, 54–58, https://doi.org/10.1038/nclimate1068, 2011.

Butterfield, N., Rowe, P. M., Stewart, E., Roesel, D., and Neshyba, S.: Quantitative three-dimensional ice roughness from scanning electron microscopy, Journal of Geophysical Research: Atmospheres, 122, 3023–3041, https://doi.org/10.1002/2016JD026094, 2017.

https://doi.org/10.5194/egusphere-2026-4436
Preprint. Discussion started: 23 September 2026

C. Labonnote, L., Brogniez, G., Doutriaux-Boucher, M., Buriez, J.-C., Gayet, J.-F., and Chepfer, H.: Modeling of light scattering in cirrus clouds with inhomogeneous hexagonal monocrystals. Comparison with in-situ and ADEOS-POLDER measurements, Geophysical Research Letters, 27, 113–116, https://doi.org/https://doi.org/10.1029/1999GL010839, 2000.

Charney, J. G., Arakawa, A., Baker, D. J., Bolin, B., Dickinson, R. E., Goody, R. M., Leith, C. E., Stommel, H. M., and Wunsch, C. I.: Carbon Dioxide and Climate: A Scientific Assessment, Tech. rep., National Academy of Sciences, Washington, DC, 1979.

Cole, B. H., Yang, P., Baum, B. A., Riedi, J., and Labonnote, L. C.: Ice particle habit and surface roughness derived from PARASOL polarization measurements, Atmospheric Chemistry and Physics, 14, 3739–3750, https://doi.org/10.5194/acp-14-3739-2014, 2014.

Dapogny, C., Dobrzynski, C., and Frey, P.: Three-dimensional adaptive domain remeshing, implicit domain meshing, and applications to free and moving boundary problems, Journal of Computational Physics, 262, 358–378, https://doi.org/10.1016/j.jcp.2014.01.005, 2014.

Donovan, D. P., van Zadelhoff, G.-J., and Wang, P.: The EarthCARE lidar cloud and aerosol profile processor (A-PRO): the A-AER, A-EBD, A-TC, and A-ICE products, Atmospheric Measurement Techniques, 17, 5301–5340, https://doi.org/10.5194/amt-17-5301-2024, 2024.

Hamel, A., Schnaiter, M., Saito, M., Wagner, R., and Järvinen, E.: Cloud Chamber Studies on the Linear Depolarisation Ratio of Small Cirrus Ice Crystals, Atmospheric Chemistry and Physics, 26, 1277–1300, https://doi.org/10.5194/acp-26-1277-2026, 2026.

Harrington, J. Y., Suber, K., and Matus, A. V.: The dependence of cirrus crystal fall speeds on shape and size, Proceedings of the American Meteorological Society, 2009.

Hess, M. W. and Wiegner, M.: COP: a data library of optical properties of hexagonal ice crystals, Applied Optics, 33, 7740–7746, https://doi.org/10.1364/AO.33.007740, 1994.

Hesse, E., Taylor, L., Collier, C., Penttilö, A., Nousiainen, T., and Ulanowski, Z.: Discussion of a physical optics method and its application to absorbing smooth and slightly rough hexagonal prisms, J. Quant. Spectrosc. Radiat. Transfer., 218, 54–67, 2018.

Heymsfield, A. J., Winker, D., Avery, M., Vaughan, M., Diskin, G., Deng, M., Mitev, V., and Matthey, R.: Relationships between Ice Water Content and Volume Extinction Coefficient from In Situ Observations for Temperatures from 0° to -86°C: Implications for Spaceborne Lidar Retrievals, Journal of Applied Meteorology and Climatology, 53, 479–505, https://doi.org/10.1175/JAMC-D-13-087.1, 2014.

Hioki, S., Yang, P., Baum, B. A., Platnick, S., Meyer, K. G., King, M. D., and Riedi, J.: Degree of ice particle surface roughness inferred from polarimetric observations, Atmospheric Chemistry and Physics, 16, 7545–7558, https://doi.org/10.5194/acp-16-7545-2016, 2016.

IPCC: Climate Change 2021: The Physical Science Basis. Contribution of Working Group I to the Sixth Assessment Report of the Intergovernmental Panel on Climate Change, https://doi.org/10.1017/9781009157896, 2021.

Irbah, A., Delanoë, J., van Zadelhoff, G.-J., Donovan, D. P., Kollias, P., Wandinger, U., and Illingworth, A. J.: The classification of atmospheric hydrometeors and aerosols from the EarthCARE radar and lidar: the A-TC, C-TC and AC-TC products, Atmospheric Measurement Techniques, 16, 2711–2734, https://doi.org/10.5194/amt-16-2711-2023, 2023.

Järvinen, E. and Schnaiter, F. M.: Low and consistent asymmetry parameters in Arctic and mid-latitude cirrus, Atmospheric Chemistry and Physics, 26, 2465–2486, https://doi.org/10.5194/acp-26-2465-2026, 2026.

Jourdan, O., Oshchepkov, S., Shcherbakov, V., Gayet, J.-F., and Isaka, H.: Assessment of cloud optical parameters in the solar region: Retrievals from airborne measurements of scattering phase functions, Journal of Geophysical Research: Atmospheres, 108, https://doi.org/https://doi.org/10.1029/2003JD003493, 2003.

Järvinen, E., Jourdan, O., Neubauer, D., Yao, B., Liu, C., Andreae, M. O., Lohmann, U., Wendisch, M., McFarquhar, G. M., Leisner, T., and Schnaiter, M.: Additional global climate cooling by clouds due to ice crystal complexity, Atmospheric Chemistry and Physics, 18, 15 767–15 781, https://doi.org/10.5194/acp-18-15767-2018, 2018a.

https://doi.org/10.5194/egusphere-2026-4436
Preprint. Discussion started: 23 September 2026

Järvinen, E., Wernli, H., and Schnaiter, M.: Investigations of Mesoscopic Complexity of Small Ice Crystals in Midlatitude Cirrus, Geophysical Research Letters, 45, https://doi.org/10.1029/2018GL079079, 2018b.

Järvinen, E., van Diedenhoven, B., Magee, N., Neshyba, S., Schnaiter, M., Xu, G., Jourdan, O., Delene, D., Waitz, F., Lolli, S., and Kato, S.: Ice Crystal Complexity and Link to the Cirrus Cloud Radiative Effect, chap. 3, pp. 47–85, American Geophysical Union (AGU), ISBN 9781119700357, https://doi.org/https://doi.org/10.1002/9781119700357.ch3, 2023.

Konoshonkin, A. V., Kustova, N. V., and Borovoi, A. G.: Beam-splitting code for light scattering by ice crystal particles within geometric-optics approximation, Journal of Quantitative Spectroscopy and Radiative Transfer, 164, 175–183, https://doi.org/https://doi.org/10.1016/j.jqsrt.2015.06.008, 2015.

Korolev, A. V., Isaac, G. A., and Hallett, J.: Ice particle habits in Arctic clouds, Geophysical Research Letters, 26, 1299–1302, https://doi.org/10.1029/1999GL900232, 1999.

Lawson, R. P., Woods, S., and Morrison, H.: A Review of Ice Particle Shapes in Cirrus formed In Situ and in Anvils, Journal of Geophysical Research: Atmospheres, 124, 10 049–10 090, https://doi.org/10.1029/2018JD030122, 2019.

Li, Q. and Groß, S.: Satellite observations of seasonality and long-term trends in cirrus cloud properties over Europe: investigation of possible aviation impacts, Atmospheric Chemistry and Physics, 22, 15 963–15 980, https://doi.org/10.5194/acp-22-15963-2022, 2022.

Macke, A., Mueller, J., and Raschke, E.: Single Scattering Properties of Atmospheric Ice Crystals, Journal of Atmospheric Sciences, 53, 2813 – 2825, https://doi.org/10.1175/1520-0469(1996)053<2813:SSPOAI>2.0.CO;2, 1996.

Magee, N., Boaggio, K., Staskiewicz, S., Lynn, A., Zhao, X., Tusay, N., Schuh, T., Bandamede, M., Bancroft, L., Connelly, D., Hurler, K., Miner, B., and Khoudary, E.: Captured cirrus ice particles in high definition, Atmospheric Chemistry and Physics, 21, 7171–7185, https://doi.org/10.5194/acp-21-7171-2021, 2021.

Markkanen, J. and Penttilä, A.: Extension of Radiative Transfer Coherent Backscattering RT-CB code to dense discrete random media, Journal of Quantitative Spectroscopy and Radiative Transfer, 310, 108 733, https://doi.org/10.1016/j.jqsrt.2023.108733, 2023.

McCall, D. S.: Measurement and modelling of light scattering by small to medium size parameter airborne particles, Ph.D. thesis, University of Hertfordshire, 2011.

Mishchenko, M. I. and Sassen, K.: Depolarization of lidar returns by small ice crystals: An application to contrails, Geophysical Research Letters, 25, 309–312, https://doi.org/10.1029/97GL03764, 1998.

Mishchenko, M. I., Hovenier, J. W., and Travis, L. D.: Light Scattering by Nonspherical Particles, Academic Press, 1999.

Muinonen, K.: Coherent backscattering of light by complex random media of spherical scatterers: numerical solution, Waves in Random Media, 14, 365–388, https://doi.org/10.1088/0959-7174/14/3/010, 2004.

Muinonen, K., Lumme, K., Peltoniemi, J., and Irvine, W. M.: Light scattering by randomly oriented crystals, Appl. Opt., 28, 3051–3060, https://doi.org/10.1364/AO.28.003051, 1989.

Muinonen, K., Mishchenko, M. I., Dlugach, J. M., Zubko, E., Penttilä, A., and Videen, G.: Coherent Backscattering Verified Numerically for a Finite Volume of Spherical Particles, The Astrophysical Journal, 760, 118, https://doi.org/10.1088/0004-637X/760/2/118, 2012.

Neshyba, S., Lowen, B., Benning, M., Lawson, A., and Rowe, P. M.: Roughness metrics of prismatic facets of ice, Journal of Geophysical Research: Atmospheres, 118, 3309–3318, https://doi.org/10.1002/jgrd.50357, 2013.

Okamoto, H., Sato, K., Borovoi, A., Ishimoto, H., Masuda, K., Konoshonkin, A., and Kustova, N.: Interpretation of lidar ratio and depolarization ratio of ice clouds using spaceborne high-spectral-resolution polarization lidar, Optics Express, 27, 36 587–36 600, https://doi.org/10.1364/OE.27.036587, 2019.

Okamoto, H., Sato, K., Borovoi, A., Ishimoto, H., Masuda, K., Konoshonkin, A., and Kustova, N.: Wavelength dependence of ice cloud backscatter properties for space-borne polarization lidar applications, Optics Express, 28, 29 178–29 191, https://doi.org/10.1364/OE.400510, 2020.

Qu, Z., Donovan, D. P., Barker, H. W., Cole, J. N. S., Shephard, M. W., and Huijnen, V.: Numerical model generation of test frames for pre-launch studies of EarthCARE's retrieval algorithms and data management system, Atmospheric Measurement Techniques, 16, 4927–4946, https://doi.org/10.5194/amt-16-4927-2023, 2023.

Saito, M. and Yang, P.: Quantifying the Impact of the Surface Roughness of Hexagonal Ice Crystals on Backscattering Properties for Lidar-Based Remote Sensing Applications, Geophysical Research Letters, 50, e2023GL104 175, https://doi.org/10.1029/2023GL104175, 2023.

Saito, M., Iwabuchi, H., Yang, P., Tang, G., King, M. D., and Sekiguchi, M.: Ice particle morphology and microphysical properties of cirrus clouds inferred from combined CALIOP-IIR measurement, Journal of Geophysical Research: Atmospheres, 122, 4440–4462, https://doi.org/10.1002/2016JD026080, 2017.

Sato, K., Okamoto, H., and Ishimoto, H.: The CPR_CLP, AC_CLP, and ACM_CLP products, Atmospheric Measurement Techniques, 18, 1325–1338, https://doi.org/10.5194/amt-18-1325-2025, 2025.

Schnaiter, F. M. and Järvinen, E.: Evidence for sub-wavelength-scale ice crystal surface roughness from single-particle light-scattering measurements, Journal of Quantitative Spectroscopy and Radiative Transfer, 359, 109 935, https://doi.org/https://doi.org/10.1016/j.jqsrt.2026.109935, 2026.

Schnaiter, M., Järvinen, E., Vochezer, P., Abdelmonem, A., Wagner, R., Jourdan, O., Mioche, G., Shcherbakov, V. N., Schmitt, C. G., Tricoli, U., Ulanowski, Z., and Heymsfield, A. J.: Cloud chamber experiments on the origin of ice crystal complexity in cirrus clouds, Atmospheric Chemistry and Physics, 16, 5091–5110, https://doi.org/10.5194/acp-16-5091-2016, 2016.

Schnaiter, M., Järvinen, E., Abdelmonem, A., and Leisner, T.: PHIPS-HALO: the airborne Particle Habit Imaging and Polar Scattering probe – Part 2: Characterization, Atmospheric Measurement Techniques, 11, 341–357, https://doi.org/10.5194/amt-11-341-2018, 2018.

Ulanowski, Z., Hesse, E., Kaye, P. H., and Baran, A. J.: Light scattering by complex ice-analogue crystals, Journal of Quantitative Spectroscopy and Radiative Transfer, 100, 382–392, https://doi.org/10.1016/j.jqsrt.2005.11.052, 2006.

Ulanowski, Z., Kaye, P. H., Hirst, E., Greenaway, R. S., Cotton, R. J., Hesse, E., and Collier, C. T.: Incidence of rough and irregular atmospheric ice particles from Small Ice Detector 3 measurements, Atmospheric Chemistry and Physics, 14, 1649–1662, https://doi.org/10.5194/acp-14-1649-2014, 2014.

van Diedenhoven, B.: Remote Sensing of Crystal Shapes in Ice Clouds, in: Springer Series in Light Scattering, Volume 2: Light Scattering, Radiative Transfer and Remote Sensing, edited by Kokhanovsky, A., pp. 197–250, Springer International, https://doi.org/10.1007/978-3-319-70808-9_5, 2018.

Voigtländer, J., Chou, C., Biber, H., Hammer, S. E., Jarvinen, E., Schnaiter, M., Schmale, J., Simonaitis, P., Bellouin, N., Hoose, C., Möhler, O., and Kiselev, A. A.: Surface roughness during depositional growth and sublimation of ice crystals, Atmospheric Chemistry and Physics, 18, 13 687–13 702, https://doi.org/10.5194/acp-18-13687-2018, 2018.

Warren, S. G. and Brandt, R. E.: Optical constants of ice from the ultraviolet to the microwave: A revised compilation, Journal of Geophysical Research: Atmospheres, 113, https://doi.org/https://doi.org/10.1029/2007JD009744, 2008.

Wehr, T., Kubota, T., Tzeremes, G., Wallace, K., Nakatsuka, H., Ohno, Y., Koopman, R., Borde, S., Eisinger, M., Ulrich, M., Lefèvre, F., Koike, M., and Okamoto, H.: The EarthCARE mission – science and system overview, Atmospheric Measurement Techniques, 16, 3581–3608, https://doi.org/10.5194/amt-16-3581-2023, 2023.

https://doi.org/10.5194/egusphere-2026-4436
Preprint. Discussion started: 23 September 2026

Yang, P. and Liou, K. N.: Geometric-optics–integral-equation method for light scattering by nonspherical ice crystals, Applied Optics, 35, 6568–6584, 1996.

Yang, P., Bi, L., Baum, B. A., Liou, K.-N., Kattawar, G. W., Mishchenko, M. I., and Cole, B.: Spectrally Consistent Scattering, Absorption, and Polarization Properties of Atmospheric Ice Crystals at Wavelengths from 0.2 to 100 µm, Journal of the Atmospheric Sciences, 70, 330 – 347, https://doi.org/https://doi.org/10.1175/JAS-D-12-039.1, 2013.

Yi, B., Yang, P., Baum, B. A., L'Ecuyer, T., Oreopoulos, L., Mlawer, E. J., Heymsfield, A. J., and Liou, K.-N.: Influence of ice particle surface roughening on the global cloud radiative effect, Journal of the Atmospheric Sciences, 73, 325–341, https://doi.org/10.1175/JAS-D-15-0265.1, 2016.

Yurkin, M. A. and Hoekstra, A. G.: The discrete-dipole-approximation code ADDA: Capabilities and known limitations, Journal of Quantitative Spectroscopy and Radiative Transfer, 112, 2234–2247, https://doi.org/https://doi.org/10.1016/j.jqsrt.2011.01.031, polarimetric Detection, Characterization, and Remote Sensing, 2011.

Zhou, C.: Coherent backscatter enhancement in single scattering, Optics Express, 26, A508–A519, https://doi.org/10.1364/OE.26.00A508, 2018.

Zhou, C. and Yang, P.: Backscattering peak of ice cloud particles, Optics Express, 23, 11 995–12 003, https://doi.org/10.1364/OE.23.011995, 2015.

Zhou, C., Huang, H., and Bi, L.: Simulation of backscattering phase function with the geometric optics method using a paired ray-tracing technique, Journal of Quantitative Spectroscopy and Radiative Transfer, 334, 109 341, https://doi.org/10.1016/j.jqsrt.2025.109341, 2025.